Overcoming the Electroluminescence Efficiency Limitations of Perovskite Light-Emitting Diodes

Authors: Himchan Cho[1†], Su-Hun Jeong[1†], Min-Ho Park[1†], Young-Hoon Kim[1], Christoph Wolf[1], Chang-Lyoul Lee[2], Jin Hyuck Heo[3], Aditya Sadhanala[4], NoSoung Myoung[2], Seunghyup Yoo[5], Sang Hyuk Im[3], Richard H. Friend[4], Tae-Woo Lee[1,6]*

Affiliation:

[1] Department of Materials Science and Engineering, Pohang University of Science and Technology (POSTECH), 77 Cheongam-Ro, Pohang, Gyungbuk 790-784, Republic of Korea.

[2] Advanced Photonics Research Institute (APRI), Gwangju Institute of Science & Technology (GIST), 1 Oryong-dong, Buk-gu, Gwangju, 500-712, Republic of Korea.

[3] Department of Chemical Engineering, College of Engineering, Kyung Hee University, 1 Seochon-dong, Giheung-gu, Youngin-si, Gyeonggi-do 446-701, Republic of Korea.

[4] Cavendish Laboratory, University of Cambridge, JJ Thomson Avenue, Cambridge CB3 0HE, UK.

[5] Department of Electrical Engineering, Korea Advanced Institute of Science and Technology (KAIST), 373-1 Guseong-dong, Daejeon 305-701.

[6] Department of Chemical Engineering, Division of Advanced Materials Science, School of Environmental Science and Engineering, Pohang University of Science and Technology (POSTECH), 77 Cheongam-Ro, Nam-Gu, Pohang, Gyungbuk 790-784, Republic of Korea.

*Corresponding author. E-mail: twlee@postech.ac.kr, taewlees@gmail.com

†: These authors contributed equally to this work.

Abstract: Organic-inorganic hybrid perovskites are emerging low-cost emitters with very high color purity, but their low luminescent efficiency is a critical drawback. We boosted the current efficiency (CE) of perovskite LEDs with a simple bilayer structure to 42.9 candela per ampere, similar to CE of phosphorescent OLEDs, with two modifications. We prevented the formation of metallic Pb atoms that cause significant exciton quenching through small increase in methylammonium bromide (MABr) molar proportion, and we spatially confined the exciton in uniform $MAPbBr_3$ nanograins (average diameter = 99.7 nanometers) formed by a nanocrystal pinning process and concomitant reduction of exciton diffusion length to 67 nanometers. These changes caused substantial increases in steady-state photoluminescence intensity and lifetime of $MAPbBr_3$ nanograin layers.

One Sentence Summary: Ultrahigh-efficiency organic/inorganic hybrid perovskite light-emitting diodes of 42.9 cd A^{-1} was achieved using stoichiometric tuning and nanograin engineering.

Main Text: Organic-inorganic hybrid perovskites (OIPs) have recently established as important class of materials in photovoltaic devices with rapid progress in increasing their power conversion efficiency (*1-5*). OIPs are being emerged also as promising light emitters because they can provide very high color purity (full width at half maximum ~ 20 nm) irrespective of the crystal size, unlike conventional inorganic quantum dots, because their intrinsic crystal structure is similar to a multiple quantum well (*6, 7*). Also, OIPs have low material cost and simply-

tunable band gap with a reasonable ionization energy (IE) comparable to common hole injection materials (*7-11*). Thus, OIPs are attractive materials as alternative emitters that can overcome the disadvantages of organic light-emitting diodes (OLEDs) (e.g., complex synthesis, high cost, and poor color purity) and inorganic quantum dot LEDs (e.g., complex synthesis, high cost and high IE).

Bright electroluminescence (EL) (> 100 cd m^{-2}) at room temperature from perovskite light-emitting diodes (PeLEDs) with methylammonium lead halides (MAPbX$_3$, where X is I, Br or Cl) emission layer was demonstrated recently (*6,7,12-18*). As an emission layer, MAPbBr$_3$ has higher air stability (*7, 19*) and exciton binding energy (76 or 150 meV) than does MAPbI$_3$ (30 or 50 meV) (*20, 21*). However, PeLEDs have much lower current efficiency (CE) at room temperature than do OLEDs or quantum dot LEDs. Existing methods have not overcome the substantial luminescence quenching in MAPbX$_3$ caused by facile thermal ionization of excitons generated in the OIP layer, which has a low exciton binding energy. Spin-coating of MAPbBr$_3$ solution creates a rough, non-uniform surface with many cuboids with large grain size (*22*), which leads to a substantial leakage current and large exciton diffusion length L_D that reduces CE in PeLEDs. To improve the CE of PeLEDs, the OIP grain size must be decreased, and OIP films should be flat and uniform. Smaller grains can spatially limit L_D of excitons or charge carriers and reduce the possibility of exciton dissociation into carriers. This fabrication goal differs from that of the OIP layers in solar cells, which should be dense films with large grain size to achieve good exciton diffusion and dissociation. Thus, processes designed to achieve uniform OIP film morphology with large grain size in solar cells such as solvent dripping (*23, 24*) are not applicable to PeLEDs, which require small L_D.

Here, we report a systematic approach for achieving highly bright and efficient green PeLEDs with CE = 42.9 cd A^{-1} and external quantum efficiency (EQE) = 8.53 % even in a simplified bilayer structure. These high efficiencies represent >20,000-fold increase compared with that of the control devices and are higher than the best EQE of a previous report regarding visible PeLEDs using OIP films by factors of > 10.6 (Table S1, Fig. S1) (*15*). The high efficiency PeLEDs were constructed based on effective management of exciton quenching by a modified MAPbBr$_3$ emission layer that was achieved using (i) fine and controllable stoichiometry modification and (ii) optimized nanograin engineering by nanocrystal pinning (NCP) (Fig. S2). Furthermore, we demonstrated a flexible PeLED using a self-organized conducting polymer (SOCP) anode and the first large-area PeLED (2 cm by 2 cm pixel).

A fundamental problem that must be solved to achieve high CE in PeLEDs is minimizing the presence of metallic Pb atoms in MAPbBr$_3$ that limits the efficiency of PeLEDs. Metallic Pb atoms can emerge in MAPbBr$_3$ even if MABr and PbBr$_2$ are mixed with 1:1 (mol:mol) ratios because of the decomposition of MABr or incomplete reaction between MABr and PbBr$_2$ (*7, 19*). Excess Pb atoms degrade luminescence by increasing the nonradiative decay rate and decreasing the radiative decay rate (*25*). Prevention of the formation of metallic Pb atoms was achieved by finely increasing the molar proportion of MABr by 2 to 7 % in MAPbBr$_3$ solution (Fig. S2A). Use of excess MABr suppressed exciton quenching and reduced hole-injection barrier from SOCP layers (Table S2) to MAPbBr$_3$ layers with decreased IE and greatly increased steady-state photoluminescence (PL) intensity and PL lifetime of MAPbBr$_3$ films. We propose that radiative decay of the PL process in MAPbBr$_3$ nanograins originates from shallow-trap-assisted radiative recombination at grain boundaries and radiative recombination inside the grains. Second, the CE in PeLEDs can be increased by decreasing MAPbBr$_3$ grain sizes, which improves uniformity and

coverage of MAPbBr$_3$ nanograin layers and radiative recombination by confining the excitons in the nanograins (leading to small L_D). An optimized NCP process (Fig. S3) helped change in the morphology of MAPbBr$_3$ layers from scattered micrometer-sized cuboids to well-packed nanograins with uniform coverage, which greatly reduced leakage current and increased CE.

We fabricated MAPbBr$_3$ films by spin-coating using stoichiometrically-modified perovskite solutions on prepared glass/SOCPs or silicon wafer/SOCPs substrates later used in devices (Fig. 1, A and B), and then characterized the films' morphologies and optoelectronic properties. The solutions had different molar ratios of MABr to PbBr$_2$ (MABr:PbBr$_2$ = 1.05:1, 1:1, or 1:1.05). To achieve uniform surface coverage and reduced grain size, NCP was used instead of normal spin-coating (Fig. S3). This process washed out the "good" solvents [dimethylformamide or dimethyl sulfoxide (DMSO)], and causes pinning of NCs by inducing fast crystallization. Chloroform was chosen as the solvent for NCP because a highly volatile nonpolar solvent is suitable to reduce the size and increase the uniformity of MAPbBr$_3$ grains by reducing solvent evaporation time. In addition, to further reduce grain size, we devised additive-based NCP (A-NCP) which uses an organic small molecule, 2,2',2"-(1,3,5-benzinetriyl)-tris(1-phenyl-1-H-benzimidazole) (TPBI), as an additive to chloroform, whereas pure chloroform is used in solvent-based NCP (S-NCP).

Use of NCP affected film morphology (Fig. 2). Without NCP, micrometer-sized MAPbBr$_3$ cuboids were scattered on the SOCP layer (Fig. 2A). They were only interconnected with a few other cuboids, and so a large amount of space remained uncovered. This high surface roughness and the formation of pinholes in OIP films result in formation of bad interface with the electron transport layer and electrical shunt paths, and thus severely limit CE in PeLEDs. In contrast, when NCP was used, perfect surface coverage was obtained, and the MAPbBr$_3$ crystal morphology changed to a well-packed assembly of tiny grains ranging from 100 to 250 nm (Fig. 2, B to E, Fig. S4). MAPbBr$_3$ grain size was little affected by the stoichiometric modification of MAPbBr$_3$ solutions (Fig. 2, B to D, Fig. S4, A to C). Furthermore, MAPbBr$_3$ grain size was further reduced to 50-150 nm (average = 99.7 nm) by A-NCP (Fig. 2E, Fig. S4D). This reduction can be attributed to hindrance of crystal growth by TPBI molecules during crystal pinning. The thickness of MAPbBr$_3$ layer was ~400 nm (Fig. 1B).

The crystal structures of MAPbBr$_3$ films were analyzed by measuring x-ray diffraction (XRD) patterns (Fig. 2F, Fig. S5, Table S3). The XRD patterns of MAPbBr$_3$ films (1:1) exhibit peaks at 15.02°, 21.3°, 30.28°, 33.92°, 37.24°, 43.28° and 46.00° that can be assigned to (100), (110), (200), (210), (211), (220) and (300) planes respectively, by using Bragg's law to convert the peak positions to interplanar spacings (Fig. 2F). The lattice parameter is in accordance with a previous report (*19*), and demonstrates that MAPbBr$_3$ films had a stable cubic $Pm\overline{3}m$ phase. Using the Scherrer equation, the crystallite size was calculated to be 23.5 ± 2.0 nm, and the variation with stoichiometric change was not large (Table S3). Because the crystallite sizes were much smaller than the apparent grain sizes (Fig. 2, A to E), we conclude that all grains consisted of many crystallites. The stoichiometric changes had very little effect on the peak positions (Fig. S5A). Furthermore, A-NCP did not change the peak positions when compared to S-NCP (Fig. S5); this stability in positions indicates that the stoichiometric changes of MAPbBr$_3$ solution and the use of TPBI additive did not affect the crystal structure of MAPbBr$_3$ films.

To study chemical changes in the MAPbBr$_3$ layers fabricated using perovskite solutions with different stoichiometries, x-ray photoelectron spectroscopy (XPS) was conducted. The survey spectra showed strong peaks of Br (~ 68 eV), Pb (~ 138 and 143 eV), C (~ 285 eV) and N

(~ 413 eV); these results agree with values in previous reports (Fig. S6A) (*7, 26-28*). Systematic deconvolution of Pb4f, Br3d and N1s spectra into summations of Gaussian-Lorentzian curves revealed the nature of chemical bonds in MAPbBr$_3$ (Fig. S6, B to D, Fig. S7). The gradual increase of MABr molar proportion in the films was confirmed by observing the gradual increase in N1s peak intensities as MABr:PbBr$_2$ increased from 1:1.05 to 1.05:1 (Fig. S7, C and D) and the gradual decrease in Br:Pb atomic ratio (Supplementary Text F). In the Pb4f spectra (Fig. S6, B to F), large peaks were observed at ~138.8 and ~143.6 eV (caused by the spin orbit split) that correspond to Pb4f$_{7/2}$ and Pb4f$_{5/2}$ levels, respectively (*26-28*). Each of these peaks was associated with a smaller peak that was shifted to 1.8-eV lower binding energy; these small peaks can be assigned to metallic Pb (*26-28*). The height of peaks that represent metallic Pb decreased as MABr:PbBr$_2$ increased from 1:1.05 to 1:1 (Fig. S6, E and F); this peak was absent in the film with MABr:PbBr$_2$ = 1.05:1 (Fig. S6F). This trend indicates that the presence of metallic Pb atoms on the films was successfully prevented by fine stoichiometry control. In contrast, the high peak intensity of the metallic Pb peak in the films with MABr:PbBr$_2$ = 1:1 and 1:1.05 suggests that numerous metallic Pb atoms were formed on the film surfaces.

We measured the work functions (WFs) and IEs of the MAPbBr$_3$ films using ultraviolet photoelectron spectroscopy (UPS) (Fig. S8). The WFs were obtained by subtracting the energies at secondary cut-offs of the UPS spectra from the UV radiation energy of 21.2 eV when a Fermi level of 0 eV was the common reference for all energies. The IEs were determined by adding the WF (Fig. S8A) to the energy offset between WFs and IEs of MAPbBr$_3$ (Fig. S8B) (*29*). The IE gradually decreased with increasing MABr molar proportion from 6.01 eV in the film with MABr:PbBr$_2$ = 1:1.05 to 5.86 eV in the film with MABr:PbBr$_2$ = 1.1:1 (Fig. 1C, Table S4). The gradual decrease in IEs with decreasing PbBr$_2$ molar proportion can be understood based on the IE being greater in PbBr$_2$ than in MAPbBr$_3$ (*30*). In PeLEDs, this decrease can help alleviate hole-injection barriers from SOCP layers to MAPbBr$_3$ layers (Fig. 1C).

The luminescent properties of the MAPbBr$_3$ films were investigated by steady-state PL measurement (Fig. 3A). The measurement was conducted using a spectrofluorometer with excitation from monochromatic light with wavelength of 405 nm (xenon lamp). The MAPbBr$_3$ films fabricated from MABr:PbBr$_2$ = 1.05:1 had a ~ 5.8 times increase in PL intensity (Fig. 3A) compared with 1:1 films, and had much higher PL quantum efficiency (PLQE; 36 % vs 3 %). In addition, the reduction of grain size with A-NCP vs S-NCP increased the PL intensity by ~2.8 times. The PL intensity of the films with MABr:PbBr$_2$ = 1:1.05 was greater than in those with MABr:PbBr$_2$ = 1:1, although the PbBr$_2$ molar proportion had increased in the former. We suspect that this departure from the expected trend is due to PbBr$_2$-induced surface passivation of the film; this process reduces nonradiative recombination at the trap sites (*31*).

To understand the kinetics of excitons and free carriers in MAPbBr$_3$ films and how the presence of metallic Pb atoms affects the PL lifetime, time-correlated single-photon counting (TCSPC) measurements were conducted (Fig. 3B). The PL decay curves were fitted using a bi-exponential decay model, in which the PL lifetime is considered as the summation of fast and slow decay components that give short lifetime τ_1 and long lifetime τ_2, respectively. To investigate the quality of quenching sites, we prepared the layers (MABr:PbBr$_2$ = 1.05:1) with and without sealing with a 50-nm-thick poly(methyl methacrylate) (PMMA) layer. The fraction f_2 of τ_2 decreased from 91 % to 77 % in the film without sealing (Table S5). Oxygen and moisture can diffuse quickly into grain boundaries when the top PMMA layer is not used; oxygen or moisture at grain boundaries provides quenching sites. The fast decay is related to

trap-assisted recombination at grain boundaries, whereas the slow decay is related to radiative recombination inside the grains (Fig. S9) (*32*).

This proposition was supported by analyzing the change in τ and f of MAPbBr$_3$ films with varying stoichiometric ratio. As MABr:PbBr$_2$ increased from 1:1 to 1.05:1, the average lifetime τ_{avg} gradually increased from 12.1 to 51.0 ns (Table S5). The short τ_{avg} (12.1 ns) in the film with MABr:PbBr$_2$ = 1:1 originated from the significant reduction of τ_2. This implies that uncoordinated metallic Pb atoms at grain boundaries inhibit radiative recombination and cause strong nonradiative recombination (Fig. S9). The MAPbBr$_3$ films fabricated using PbBr$_2$-rich perovskite solution (MABr:PbBr$_2$ = 1:1.05) had a longer lifetime than films with MABr:PbBr$_2$ = 1:1, possibly through PbBr$_2$-induced surface passivation (*31*). We calculated the average L_D using a model similar to that in previous reports (Fig. S10) (*33*). The films (MABr:PbBr$_2$ = 1.05:1) underneath a PMMA layer exhibited a much smaller L_D (67 nm) than those previously reported (>1 μm) (*33, 34*). We attribute this reduction in L_D to the reduced grain sizes in which excitons are spatially stronger confined, thereby reducing dissociation and enhancing radiative recombination; this compensates the plausible adverse effect of larger grain boundary area (*6*).

The PeLED fabricated without using NCP showed poor luminous characteristics (maximum CE = 2.03×10^{-3} cd A^{-1}) mainly due to high leakage current (Fig. S11). In contrast, maximum CE was significantly increased (0.183 cd A^{-1}) when a full-coverage uniform MAPbBr$_3$ nanograin layer with decreased grain size was achieved using S-NCP (Fig. 4, A and B, Table 1). The maximum CE was boosted up to 21.4 cd A^{-1} in the PeLEDs fabricated with perovskite solutions with excess MABr (1.07:1, 1.05:1, 1.03:1 and 1.02:1) (Fig. 4A, Table 1). As MABr:PbBr$_2$ increased from 1:1 to 1.05:1, the maximum CE varied from 0.183 to 21.4 cd A^{-1}. Without stoichiometric modifications of MAPbBr$_3$ to avoid metallic Pb atoms (molar ratios 1:1 and 1:1.05), the achieved maximum CEs was only 0.183 and 4.87×10^{-2} cd A^{-1}, respectively.

We further increased CE of PeLEDs by using A-NCP. The PeLEDs based on A-NCP had a maximum CE of 42.9 cd A^{-1} (Fig. 4, C and D, Table 1), which represents an EQE of 8.53 % when the angular emission profile is considered (Fig. S12). The EL spectra of PeLEDs were very narrow; full width at half maximum was ~20 nm for all spectra; this high color purity of OIP emitters show great potential when used in displays (Fig. 4E). A pixel of the PeLED of based on MABr:PbBr$_2$ = 1.05:1 exhibited strong green light emission (Fig. S13A). Furthermore, the proposed processes and materials used therein are compatible with flexible and large-area devices; a high-brightness flexible PeLED (Fig. 4, F and G) and a large-area (2 cm by 2 cm pixel) PeLED (Fig. S13B) were fabricated. Our study reduces the technical gap between PeLEDs and OLEDs or quantum dot LEDs, and is a big leap towards the development of efficient next-generation emitters with high color purity and low fabrication cost based on perovskites.

References and Notes:

1. W. S. Yang, J. H. Noh, N. J. Jeon, Y. C. Kim, S. Ryu, J. Seo, S. I. Seok, High-performance photovoltaic perovskite layers fabricated through intramolecular exchange. *Science* **348**, 1234-1237 (2015).

2. M. Liu, M. B. Johnston, H. J. Snaith, Efficient planar heterojunction perovskite solar cells by vapour deposition. *Nature* **501**, 395-398 (2013).

3. N. J. Jeon, J. H. Noh, W. S. Yang, Y. C. Kim, S. Ryu, J. Seo, S. I. Seok, Compositional

engineering of perovskite materials for high-performance solar cells. *Nature* **517**, 476-480 (2015).

4. J.-H. Im, I.-H. Jang, N. Pellet, M. Grätzel, N.-G. Park, Growth of $CH_3NH_3PbI_3$ cuboids with controlled size for high-efficiency perovskite solar cells. *Nat. Nanotechnol.* **9**, 927-932 (2014).

5. J.-Y. Jeng, K.-C. Chen, T.-Y. Chiang, P.-Y. Lin, T.-D. Tsai, Y.-C. Chang, T.-F. Guo, P. Chen, T.-C. Wen, Y.-J. Hsu, Nickel oxide electrode interlayer in $CH_3NH_3PbI_3$ perovskite/PCBM planar-heterojunction hybrid solar cells. *Adv. Mater.* **26**, 4107-4113 (2014).

6. Z.-K. Tan, R. S. Moghaddam, M. L. Lai, P. Docampo, R. Higler, F. Deschler, M. Price, A. Sadhanala, L. M. Pazos, D. Credgington, F. Hanusch, T. Bein, H. J. Snaith, R. H. Friend, Bright light-emitting diodes based on organometal halide perovskite. *Nat. Nanotechnol.* **9**, 687-692 (2014).

7. Y.-H. Kim, H. Cho, J. H. Heo, T.-S. Kim, N. Myoung, C.-L. Lee, S. H. Im, T.-W. Lee, Multi-colored organic/inorganic hybrid perovskite light-emitting diodes. *Adv. Mater.* **27**, 7, 1248-1254 (2015).

8. D. B. Mitzi, Synthesis, crystal structure, and optical and thermal properties of $(C_4H_9NH_3)_2MI_4$ (M = Ge, Sn, Pb). *Chem. Mater.* **8**, 791-800 (1996).

9. M. R. Filip, G. E. Eperon, H. J. Snaith, F. Giustino, Steric engineering of metal-halide perovskites with tunable optical band gaps. *Nat. Commun.* **5**, 5757 (2014).

10. T. M. Koh, K. Fu, Y. Fang, S. Chen, T. C. Sum, N. Mathews, S. G. Mhaisalkar, P. P. Boix, T. Baikie, Formamidinium-containing metal-halide: an alternative material for near-IR absorption perovskite solar cells. *J. Phys. Chem. C.* **118**, 16458-16462 (2014).

11. G. E. Eperon, S. D. Stranks, C. Menelaou, M. B. Johnston, L. M. Herz, H. J. Snaith, Formamidinium lead trihalide: a broadly tunable perovskite for efficient planar heterojunction solar cells. *Energy Environ. Sci.* **7**, 982-988 (2014).

12. R. L. Z. Hoye, M. R. Chua, K. P. Musselman, G. Li, M.-L. Lai, Z.-K. Tan, N. C. Greenham, J. L. MacManus-Driscoll, R. H. Friend, D. Credgington, Enhanced performance in fluorene-free organometal halide perovskite light-emitting diodes using tunable, low electron affinity oxide electron injectors. *Adv. Mater.* **27**, 1414-1419 (2015).

13. N. K. Kumawat, A. Dey, K. L. Narasimhan, D. Kabra, Near infrared to visible electroluminescent diodes based on organometallic halide perovskites: structural and optical investigation. *ACS Photonics* **2**, 349-354 (2015).

14. G. Li, Z.-K. Tan, D. Di, M. L. Lai, L. Jiang, J. H.-W. Lim, R. H. Friend, N. C. Greenham, Efficient light-emitting diodes based on nanocrystalline perovskite in a dielectric polymer matrix. *Nano Lett.* **15**, 2640-2644 (2015).

15. J. Wang, N. Wang, Y. Jin, J. Si, Z.-K. Tan, H. Du, L. Cheng, X. Dai, S. Bai, H. He, Z. Ye, M. L. Lai, R. H. Friend, W. Huang, Interfacial control toward efficient and low-voltage perovskite light-emitting diodes. *Adv. Mater.* **27**, 2311-2316 (2015).

16. A. Sadhanala, A. Kumar, S. Pathak, A. Rao, U. Steiner, N. C. Greenham, H. J. Snaith, R. H. Friend, Electroluminescence from organometallic lead halide perovskite-conjugated polymer diodes. *Adv. Electron. Mater.* **1**, 1500008 (2015).

17. J. C. Yu, D. B. Kim, G. Baek, B. R. Lee, E. D. Jung, S. Lee, J. H. Chu, D.-K. Lee, K. J. Choi, S. Cho, M. H. Song, High-performance planar perovskite optoelectronic devices: a morphological and interfacial control by polar solvent treatment. *Adv. Mater.* **27**, 3492-3500 (2015).

18. N. K. Kumawat, A. Dey, A. Kumar, S. P. Gopinathan, K. L. Narasimhan, D. Kabra, Band gap tuning of $CH_3NH_3Pb(Br_{1-x}Cl_x)_3$ hybrid perovskite for blue electroluminescence. *ACS Appl. Mater. Interfaces*, **7**, 13119–13124 (2015).

19. J. H. Noh, S. H. Im, J. H. Heo, T. N. Mandal, S. I. Seok, Chemical management for colorful, efficient, and stable inorganic-organic hybrid nanostructured solar cells. *Nano Lett.* **13**, 1764-1769 (2013).

20. I. B. Koutselas, L. Ducasse, G. C. Papavassiliou, Electronic properties of three- and low-dimensional semiconducting materials with Pb halide and Sn halide units. *J. Phys.: Condens. Matter* **8**, 1217–1227 (1996).

21. K. Tanaka, T. Takahashi, T. Ban, T. Kondo, K. Uchida, N. Miura, Comparative study on the excitons in lead-halide-based perovskite-type crystals $CH_3NH_3PbBr_3$ $CH_3NH_3PbI_3$. *Solid State Commun.* **127**, 619–623 (2003).

22. J. H. Heo, D. H. Song, S. H. Im, Planar $CH_3NH_3PbBr_3$ hybrid solar cells with 10.4% power conversion efficiency, fabricated by controlled crystallization in the spin-coating process. *Adv. Mater.* **26**, 8179-8183 (2014).

23. M. Xiao, F. Huang, W. Huang, Y. Dkhissi, Y. Zhu, J. Etheridge, A. Gray-Weale, U. Bach, Y.-B. Cheng, L. Spiccia, A fast deposition-crystallization procedure for highly efficient lead iodide perovskite thin-film solar cells. *Angew. Chem. Int. Ed.* **53**, 9898-9903 (2014).

24. N. J. Jeon, J. H. Noh, Y. C. Kim, W. S. Yang, S. Ryu, S. I. Seok, Solvent engineering for high-performance inorganic-organic hybrid perovskite solar cells. *Nat. Mater.* **13**, 897-903 (2014).

25. E. Dulkeith, M. Ringler, T. A. Klar, J. Feldmann, Gold nanoparticles quench fluorescence by phase induced radiative rate suppression. *Nano Lett.* **5**, 585-589 (2005).

26. S. Gonzalez-Carrero, R. E. Galian, J. Pérez-Prieto, Maximizing the emissive properties of $CH_3NH_3PbBr_3$ perovskite nanoparticles. *J. Mater. Chem. A* **3**, 9187-9193 (2015).

27. R. Lindblad, N. K. Jena, B. Philippe, J. Oscarsson, D. Bi, A. Lindblad, S. Mandal, B. Pal, D. D. Sarma, O. Karis, H. Siegbahn, E. M. J. Johansson, M. Odelius, H. Rensmo, Electronic structure of $CH_3NH_3PbX_3$ Perovskite: dependence on the halide moiety. *J. Phys. Chem. C* **119**, 1818-1825 (2015).

28. I. A. Shkrob, T. W. Marin, Charge trapping in photovoltaically active perovskites and related halogenoplumbate compounds. *J. Phys. Chem. Lett.* **5**, 1066-1071 (2014).

29. P. Schulz, E. Edri, S. Kirmayer, G. Hodes, D. Cahen, A. Kahn, Interface energetics in organo-metal halide perovskite-based photovoltaic cells. *Energy Environ. Sci.* **7**, 1377–1381 (2014).

30. J. Kanbe, H. Onuki, R. Onaka, Photoelectron spectra of $PbCl_2$, $PbBr_2$ and similar materials. *J. Phys. Soc. Jpn.* **43**, 1280-1285 (1977).

31. Q. Chen, H. Zhou, T.-B. Song, S. Luo, Z. Hong, H.-S. Duan, L. Dou, Y. Liu, Y. Yang,

Controllable self-induced passivation of hybrid lead iodide perovskite toward high performance solar cells. *Nano Lett.* **14**, 4158-4163 (2014).

32. D. Shi, V. Adinolfi, R. Comin, M. Yuan, E. Alarousu, A. Buin, Y. Chen, S. Hoogland, A. Rothenberger, K. Katsiev, Y. Losovyj, X. Zhang, P. A. Dowben, O. F. Mohammed, E. H. Sargent, O. M. Bakr, Low trap-state density and long carrier diffusion in organolead trihalide perovskite single crystals. *Science* **347**, 519-522 (2015).

33. S. D. Stranks, G. E. Eperon, G. Grancini, C. Menelaou, M. J. P. Alcocer, T. Leijtens, L. M. Herz, A. Petrozza, H. J. Snaith, Electron-hole diffusion lengths exceeding 1 micrometer in an organometal trihalide perovskite absorber. *Science* **342**, 341–344 (2013).

34. R. Sheng, A. Ho-Baillie, S. Huang, S. Chen, X. Wen, X. Hao, M. A. Green, Methylammonium lead bromide perovskite-based solar cells by vapor-assisted deposition. *J. Phys. Chem. C*, **119**, 3545-3549 (2015).

35. J. C. De Mello, H. F. Wittmann, R. H. Friend, An improved experimental determination of external photoluminescence quantum efficiency. *Adv. Mater.* **9**, 230–232 (1997).

36. X. Qin, H. Dong, W. Hu, Green light-emitting diode from bromine based organic-inorganic halide perovskite, *Sci. China Mater.* **58**, 186-191 (2015).

37. J. I. Langford, A. J. C. Wilson, Scherrer after sixty years: a survey and some new results in the determination of crystallite size. *J. Appl. Cryst.* **11**, 102-113 (1978).

38. J. F. Moulder, W. F. Stickle, P. E. Sobol, K. D. Bomben, *Handbook of X-ray photoelectron spectroscopy* Ch. II (Physical Electronics, Inc., Minnesota, United States of America, 1992).

39. A. F. van Driel, I. S. Nikolaev, P. Vergeer, P. Lodahl, D. Vanmaekelbergh, W. L. Vos, Statistical analysis of time-resolved emission from ensembles of semiconductor quantum dots: Interpretation of exponential decay models. *Phys. Rev. B* **75**, 035329 (2007).

40. L. Gil-Escrig, G. Longo, A. Pertegás, C. Roldán-Carmona, A. Soriano, M. Sessolo, H. J. Bolink, Efficient photovoltaic and electroluminescent perovskite devices. *Chem. Commun.* **51**, 569-571 (2015).

41. P. E. Shaw, A. Ruseckas, I. D. W. Samuel, Exciton diffusion measurements in poly(3-hexylthiophene). *Adv. Mater.* **20**, 3516–3520 (2008).

42. P. E. Shaw, Measurements of exciton diffusion in conjugated polymers. PhD Thesis, University of St Andrews (2009).

43. A. E. McKinnon, A. G. Szabo, D. R. Miller, The deconvolution of photoluminescence data. *J. Phys. Chem.* **81**, 1564–1570 (1977).
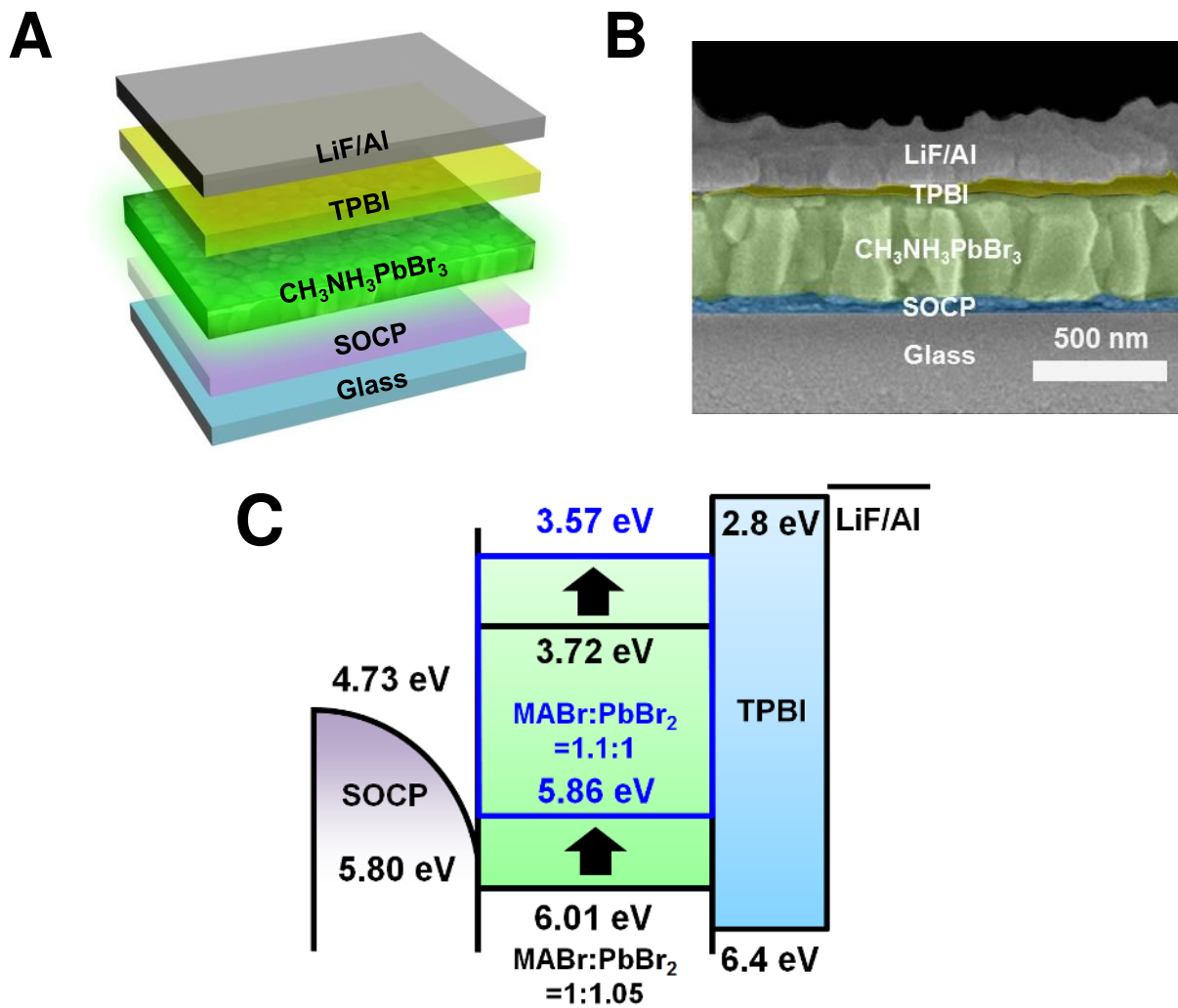
**Supplementary Materials:**

Materials and Methods

Figs. S1 to S13

Table S1 to S5

References (*35-43*)

Fig. 1. Schematic illustrations of device structure and its cross-sectional SEM image, and energy band structure. (**A**) The device structure; perovskite films were characterized without the TPBI layer and LiF/Al electrode. (**B**) Cross-sectional SEM image of PeLEDs. (**C**) Energy band diagram of PeLEDs showing decrease of IE with increasing MABr molar proportion
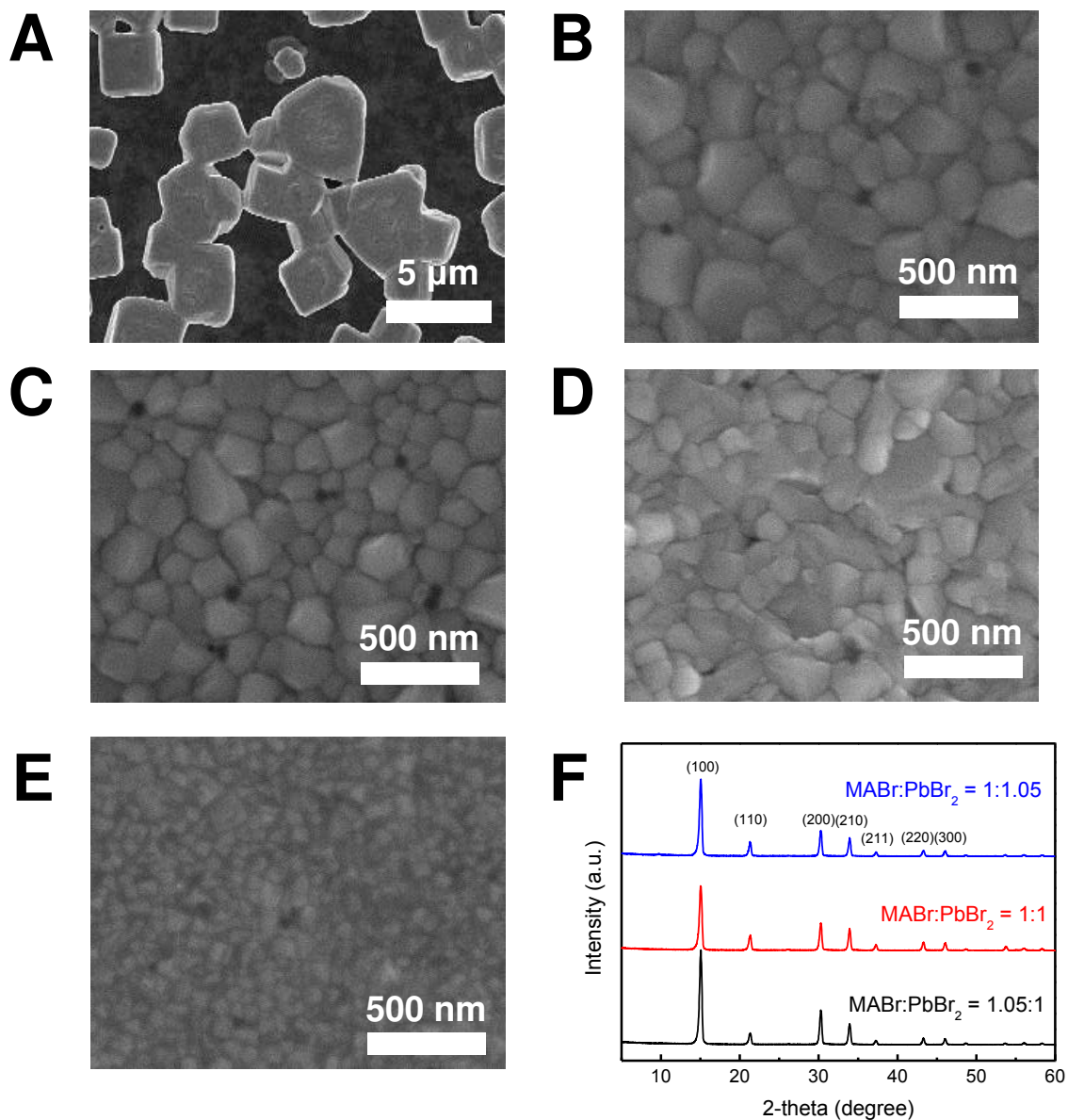
Fig. 2. SEM images and XRD patterns of MAPbBr$_3$ layers. SEM images of MAPbBr$_3$ layers of (**A**) MABr:PbBr$_2$ = 1:1 without NCP, (**B**) 1:1.05, (**C**) 1:1, (**D**) 1.05:1 with S-NCP, (**E**) 1.05:1 with A-NCP. (**F**) XRD patterns of MAPbBr$_3$ nanograin layers with MABr:PbBr$_2$ = 1:1.05, 1:1 and 1.05:1.
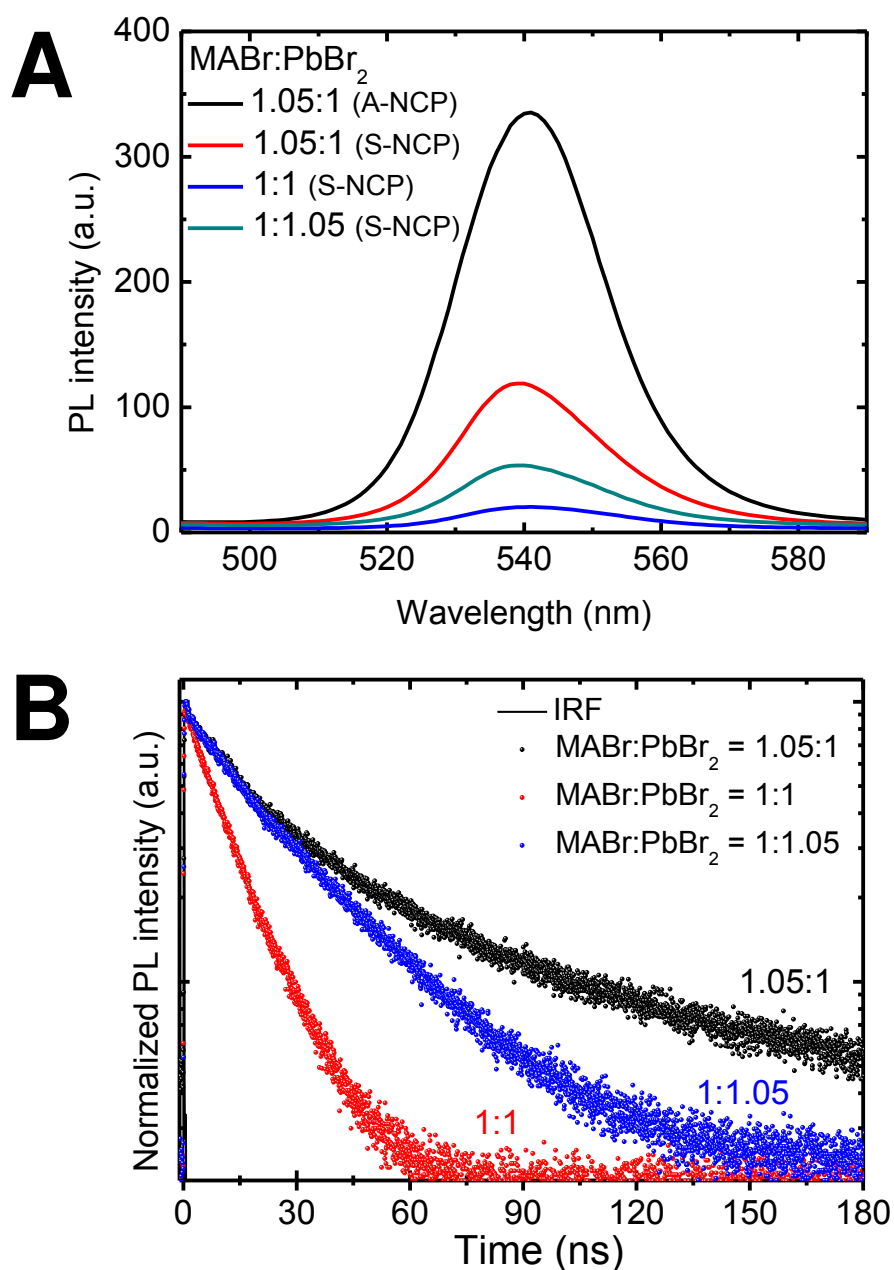
Fig. 3. Steady-state PL spectra and lifetime. (**A**) Steady-state PL spectra of MAPbBr$_3$ nanograin layers with NCP type and varying molar ratio MABr:PbBr$_2$. (**B**) PL lifetime curves of MAPbBr$_3$ nanograin layers with varying molar ratio MABr:PbBr$_2$. Black line: instrument response function (IRF).
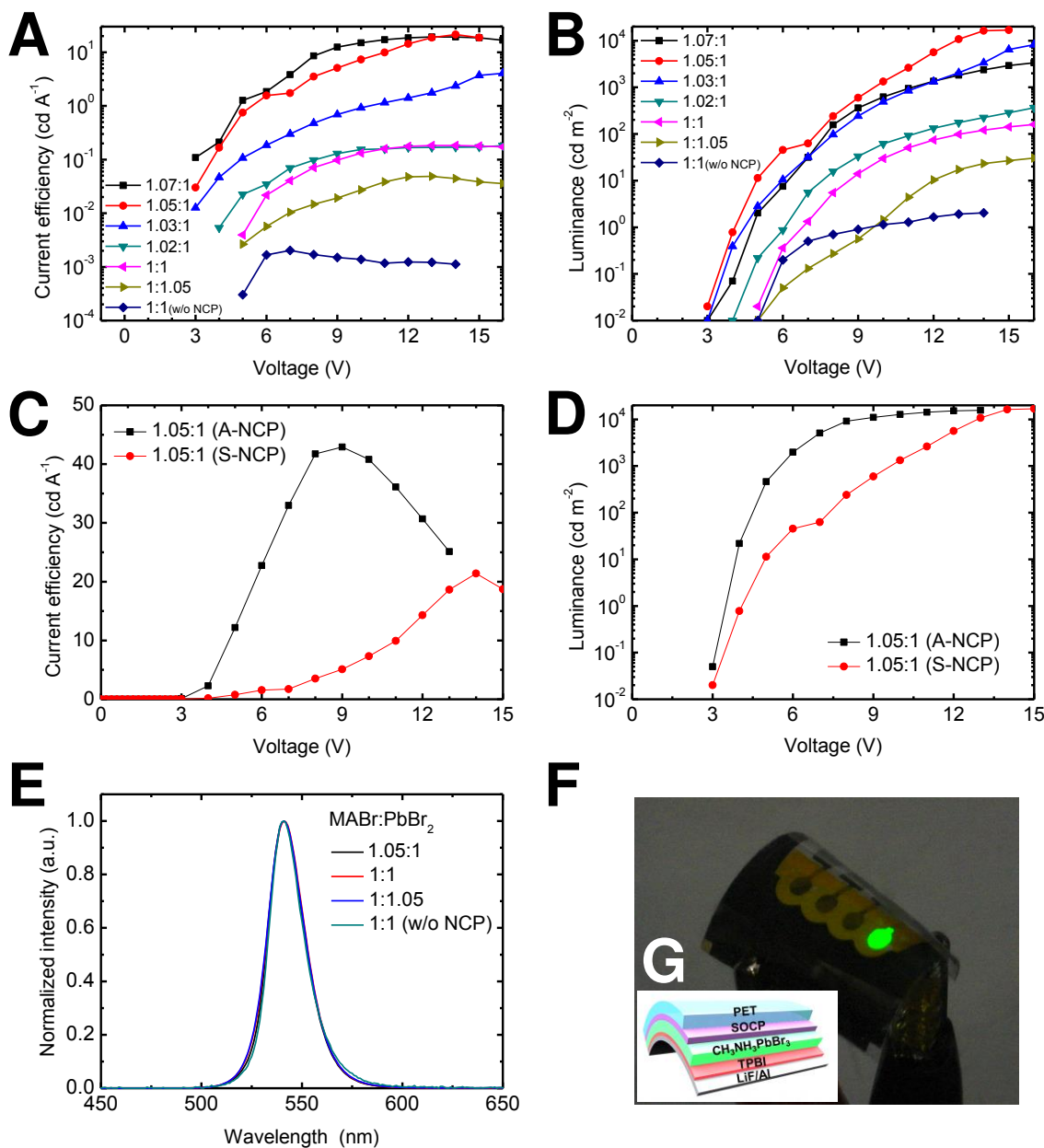
Fig. 4. PeLED characteristics, EL spectra, photograph of PeLED. (A and B) CE and luminance of PeLEDs based on S-NCP and MAPbBr$_3$ nanograin emission layers with varying molar ratio MABr:PbBr$_2$ (—■— 1.07:1 , —●— 1.05:1, —▲— 1.03:1, —▼— 1.02:1, —◀— 1:1, —▶— 1:1.05, —◆— 1:1 without NCP). **(C and D)** CE and luminance of PeLEDs based on A-NCP and MAPbBr$_3$ nanograin emission layers. **(E)** EL spectra of PeLEDs. **(F)** Photograph of a flexible PeLED, and **(G)** its device structure.

Table 1. Maximum CE of PeLEDs depending on NCP and the molar ratio MABr:PbBr$_2$.

MABr:PbBr$_2$	NCP type	Max. CE (cd A^{-1})
1.05:1	A-NCP	42.9
1.07:1		19.3
1.05:1		21.4
1.03:1	S-NCP	4.03
1.02:1		0.457
1:1		0.183
1:1.05		4.87×10^{-2}
1:1	Without NCP	2.03×10^{-3}